ADVANCED MATERIALS
www.advmat.de

# Centrifuge-Free Separation of Solution-Exfoliated 2D Nanosheets via Cross-Flow Filtration

*Julia R. Downing, Santiago Diaz-Arauzo, Lindsay E. Chaney, Daphne Tsai, Janan Hui, Jung-Woo T. Seo, Deborah R. Cohen, Michael Dango, Jinrui Zhang, Nicholas X. Williams, Justin H. Qian, Jennifer B. Dunn, and Mark C. Hersam**

**Solution-processed graphene is a promising material for numerous high-volume applications including structural composites, batteries, sensors, and printed electronics. However, the polydisperse nature of graphene dispersions following liquid-phase exfoliation poses major manufacturing challenges, as incompletely exfoliated graphite flakes must be removed to achieve optimal properties and downstream performance. Incumbent separation schemes rely on centrifugation, which is highly energy-intensive and limits scalable manufacturing. Here, cross-flow filtration (CFF) is introduced as a centrifuge-free processing method that improves the throughput of graphene separation by two orders of magnitude. By tuning membrane pore sizes between microfiltration and ultrafiltration length scales, CFF can also be used for efficient recovery of solvents and stabilizing polymers. In this manner, life cycle assessment and techno-economic analysis reveal that CFF reduces greenhouse gas emissions, fossil energy usage, water consumption, and specific production costs of graphene manufacturing by 57%, 56%, 63%, and 72%, respectively. To confirm that CFF produces electronic-grade graphene, CFF-processed graphene nanosheets are formulated into printable inks, leading to state-of-the-art thin-film conductivities exceeding $10^4$ S $m^{-1}$. This CFF methodology can likely be generalized to other van der Waals layered solids, thus enabling sustainable manufacturing of the diverse set of applications currently being pursued for 2D materials.**

## 1. Introduction

The superlative properties of two-dimensional (2D) materials (e.g., graphene, hexagonal boron nitride, and molybdenum disulfide) have led to increasing interest in their production and integration into diverse structural, electronic, and energy technologies.[1–3] While electronic-grade 2D materials can be realized through epitaxial growth,[1] this bottom-up manufacturing approach has limited scalability and thus is not viable for industrial-scale, high-volume applications. Consequently, significant effort has been devoted to liquid-phase exfoliation (LPE) as a nominally more scalable, top-down approach wherein cavitation-induced shearing exfoliates 2D nanosheets from layered van der Waals solids during ultrasonication.[4] To further improve the throughput of LPE, shear mixing and wet jet milling have emerged as alternatives to ultrasonication.[5,6] However, since LPE invariably yields incomplete exfoliation, additional lower-throughput separation steps are needed to achieve sufficient 2D nanosheet size monodispersity for high-performance applications.[1]

As the first van der Waals layered material to be exfoliated, graphene is viewed as the prototypical 2D material and has been explored most extensively for industrial applications including structural composites, batteries, sensors, and printed

J. R. Downing, S. Diaz-Arauzo, L. E. Chaney, D. Tsai, J.-W. T. Seo, N. X. Williams, J. H. Qian, M. C. Hersam
Department of Materials Science and Engineering
Northwestern University
2220 Campus Dr., Evanston, IL 60208, USA
E-mail: m-hersam@northwestern.edu

The ORCID identification number(s) for the author(s) of this article can be found under https://doi.org/10.1002/adma.202212042



**DOI: 10.1002/adma.202212042**

J. Hui, M. C. Hersam
Department of Chemistry
Northwestern University
2145 Sheridan Rd., Evanston, IL 60208, USA

D. R. Cohen, M. Dango
Cytiva
100 Results Way, Marlborough, MA 01752, USA

J. Zhang, J. B. Dunn
Department of Chemical and Biological Engineering
Northwestern University
2145 Sheridan Rd., Evanston, IL 60208, USA

electronics.[7] Printable conductive inks are among the most promising applications for graphene, but also impose the most stringent manufacturing requirements since chemical modifications to the graphene basal plane compromise electronic properties.[8–10] In addition, the electrical conductivity of printed graphene thin films depends sensitively on the morphology of the percolating network, which further implies that the constituent graphene nanosheets need to be highly monodisperse in nanoscale size.[11] Therefore, following LPE, electronic-grade graphene dispersions are invariably subjected to centrifuge-based separation (CBS) to improve graphene nanosheet size monodispersity.[12] While CBS processes such as density gradient ultracentrifugation and liquid cascade centrifugation produce highly monodisperse graphene dispersions, these methods are energy-intensive and intrinsically limited in their scalability.[13–15] Even in cases where LPE graphene from high-volume synthetic pathways is successfully printed as-is via contact-based printing techniques, the constituent flakes are too large for nozzle-based printing techniques (e.g., inkjet printing (IJP) and aerosol-jet printing (AJP)) without further purification by CBS.[15–17]

To address CBS limitations, alternative solution-based separation methods have been developed, but have been primarily applied in the biochemistry and pharmaceutical fields,[18,19] leaving their utility for 2D material separations relatively unexplored. Examples include chromatography, field-flow fractionation, force-field extraction, magnetic separation, microfiltration, and ultrafiltration.[20–25] Among these methods, microfiltration (MF) and ultrafiltration (UF) are particularly attractive for solid/liquid separation due to their relative simplicity and energy efficiency. However, conventional dead-end filtration processes (e.g., vacuum filtration) are susceptible to fouling because solid material accumulates on the filter surface. On the other hand, in cross-flow filtration (CFF), also known as tangential flow filtration, liquid flows parallel to the membrane surface, thus minimizing fouling. CFF is ideal for solid/liquid mixtures with a wide range of solids loading and small particle sizes (<5 μm).[26] During CFF, a feed dispersion of solids suspended in liquid is continuously recirculated along a porous membrane surface. The driving force for separation is the transmembrane pressure (TMP), which is orthogonal to the primary liquid flow and drives sufficiently small particles through the pores.[27,28] This stream of small particles is known as the permeate, whereas the unfiltered retentate remains in closed-loop recirculation to be further filtered with each pass through CFF.

Many geometries exist for CFF membrane modules including tubular, flat sheet, spiral-wound, and hollow-fiber configurations.[26] Charged membranes can further aid separation, resulting in an electro-filtration scheme that mitigates fouling, particularly for charged particle separation.[29] In the context of nanomaterials, CFF has been successfully applied to the removal of nanoparticle contaminants from one-dimensional (1D) nanowires in addition to achieving separation of 1D carbon nanotubes by length.[30,31] CFF has also been used to purify and concentrate graphene quantum dots and related chemically prepared or modified nanomaterials.[24,32–35] However, we note that these instances of CFF are limited to nanomaterials synthesized by bottom-up wet chemical synthesis. Furthermore, in all of these cases, CFF was operated in the standard mode where the retentate was collected for further processing and the permeate was discarded. While enrichment of large particles in the retentate is often the targeted outcome of a CFF process, we hypothesized that the permeate stream would be ideal for isolating small particles from larger aggregates, which is the primary objective of 2D material separations.

Here we invert the paradigm of CFF and focus on the permeate as the target stream to isolate monodisperse graphene nanosheets from larger, incompletely-exfoliated graphite particles. This unconventional application of CFF is enabled by operation in a regime of high cross-flow and low feed concentration, which efficiently extracts small particles with minimal membrane fouling. Furthermore, the high cross-flow leads to a turbulent flow regime that facilitates a higher pressure drop from the feed to retentate ports, prolonging successful CFF. The input graphene dispersion was prepared by LPE of graphite in the presence of ethyl cellulose (EC).[36] The use of EC as a stabilizing polymer minimizes graphene nanosheet reaggregation, enabling high-volume production of concentrated graphene dispersions in ethanol. Moreover, monodisperse graphene/EC dispersions are well-known to produce highly conductive inks, thus providing a direct means for verifying that CFF yields electronic-grade graphene[37,38] with broad applicability in printed electronics.[39–42] Since the lateral size and thickness of LPE graphene nanosheets are sufficiently correlated, the lateral size separation achieved by CFF results in flakes with the nanoscale thickness required for printable graphene inks.[43]

To demonstrate the scalability of this CFF methodology, successful graphene separation is shown using cross-flow microfiltration (CF-MF) across three volumetric orders of magnitude from the milliliter to the liter scale. The resulting graphene nanosheets exhibit comparable size distributions to CBS control samples, while achieving orders of magnitude improvement in separation throughput. Following CF-MF isolation of monodisperse graphene nanosheets, cross-flow ultrafiltration (CF-UF) with nanoscale pores is then employed to recover ethanol and EC, thereby concentrating graphene dispersions and facilitating continuous flow recycling and waste minimization. Life cycle assessment (LCA) and techno-economic analysis (TEA) confirm that CFF leads to substantial reductions in greenhouse gas emissions, fossil energy usage, water consumption, and specific production costs of graphene manufacturing. Overall, this work establishes CFF as a centrifuge-free 2D material processing paradigm with unprecedented manufacturing throughput and environmental sustainability while concurrently achieving state-of-the-art printed thin-film electrical conductivities exceeding $10^4$ S $m^{-1}$.

## 2. Results and Discussion

### 2.1. Process Overview

CFF fundamentally differs from dead-end filtration since the process mixture primarily travels tangentially across the surface of the membrane rather than directly into it. CFF requires careful consideration of multiple membrane characteristics such as geometry, pore size, surface area, and number of channels in order to achieve effective separation of the targeted material. Process parameters including membrane flux, feed concentration, and flow rates must also be precisely tuned to meet separation objec-

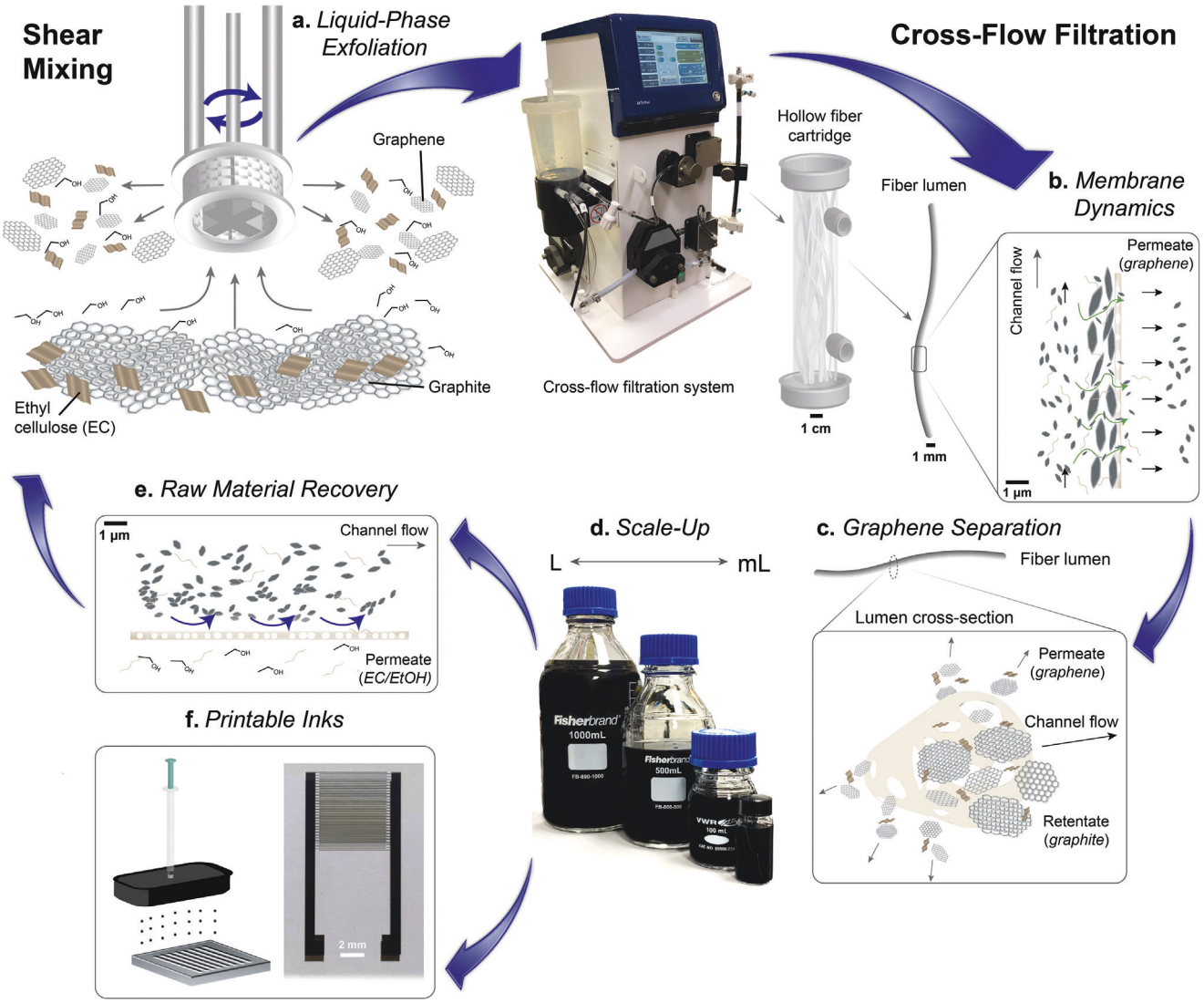


**Figure 1.** Schematic overview of the continuous-flow pathway for processing graphene nanosheets with cross-flow filtration (CFF). a) Graphite is exfoliated via shear mixing in the presence of ethanol and ethyl cellulose (EC), leading to a polydisperse sample of well-exfoliated graphene nanosheets and poorly-exfoliated graphite particles. b) Shear-mixed dispersions are processed via CFF using a hollow fiber cross-flow microfiltration module (CF-MF). c) Well-exfoliated graphene nanosheets traverse the porous membrane and are pumped out through the permeate port, while poorly-exfoliated graphite particles remain in the retentate. d) By increasing the feed flow rate and filtration surface area, CFF can be scaled to 10 L. e) Ethanol and EC recovery is achieved by a second stage of CFF that utilizes the nanoscale pores for ultrafiltration (CF-UF). f) The final graphene/EC powders are formulated into printable inks that yield thin films with high electrical conductivities exceeding $10^4$ S $m^{-1}$.

tives. A detailed discussion of the principles and considerations of CFF is provided in Section S1, Supporting Information.

Our CFF process enables a modular energy-efficient separation scheme that is specifically tailored for graphene/EC dispersions (**Figure 1**). Following LPE by shear mixing, the resulting dispersions containing poorly-exfoliated graphite, well-exfoliated graphene nanosheets, EC, and ethanol (Figure 1a) only experience natural sedimentation due to gravity prior to filtration with a CFF unit (Cytiva ÄKTA Flux s). This unit supports various filtration modules and offers process controls including tunable pump flow rates that directly modulate process pressures and filtration performance (Figure 1b). The filter modules used here contain bundles of hollow fiber membranes composed of hydrophobic polysulfone, which minimizes material interactions between the membrane and the feed dispersion.

For CF-MF process control, sensors are used to monitor the pressure at the feed, retentate, and permeate ports of the filter module. A peristaltic feed pump drives the process mixture through the module. A second peristaltic permeate pump facilitates collection of the permeate dispersion containing well-exfoliated graphene nanosheets, while the retentate stream containing poorly-exfoliated graphite is returned to the feed reservoir for additional passes through CF-MF. Here, the secondary pump is key for maintaining a constant flux across the membrane, given that the spontaneous flux is insufficient to facilitate passage of graphene nanosheets through the pores (Figure 1c).

Provided that CF-MF is carried out under optimized processing conditions, working volumes up to 10 L can be accommodated (Figure 1d). The filters can also be washed and regenerated after each experiment with pure solvent to prolong their lifetime.

The microfiltration permeate stream from CF-MF is sent into CF-UF (pore size is ≈10 nm), which enables recovery and recycling of ethanol and EC via the CF-UF permeate (Figure 1e). Meanwhile, the CF-UF retentate is enriched to an even more concentrated dispersion of monodisperse graphene nanosheets as ethanol/EC are removed. The monodisperse graphene nanosheets from the CF-MF permeate/CF-UF retentate can then be used for high-performance applications such as printable conductive inks. Regarding material quality, we note that measures of quality or utility of LPE graphene vary widely in the literature depending on the targeted application. For this reason, we focused on printable conductive inks (Figure 1f) for our demonstration of CFF as a 2D material processing method due to a clearly defined figure of merit (i.e., the electrical conductivity of the printed graphene film) in addition to the sensitivity of electronic properties to graphene nanosheet size monodispersity.

### 2.2. Membrane Dynamics and Process Control

During CF-MF, we found that the anisotropic shape of the graphene nanosheets led to a deviation from the previously reported membrane fouling behavior of other nanoparticles that have been processed with CFF.[20,30] This deviation presented a challenge to identify the optimal operating regime to mitigate fouling of solution-exfoliated 2D nanosheets. We began by targeting a membrane flux value compatible with CF-MF membranes rated with a pore size of 0.65 µm (Table S1, Supporting Information).

In CFF, flux ($J$) is the critical parameter dictating separation performance, with higher flux offering improved process throughput. In Equation (1), J is defined as the volume of solution passing through the membrane area per unit time in units of L $m^{-2}$ $h^{-1}$:

$$J = \mu \frac{\mathrm{TMP}}{R_g + R_m + R_c} \quad (1)$$

where $\mu$ is viscosity, TMP is the transmembrane pressure, and $R_g$, $R_m$, and $R_c$ correspond to the gel boundary/polarization layer resistance, membrane resistance, and concentration boundary resistance on the membrane, respectively.[28] Since it is challenging to quantitatively measure these resistances, TMP is the most readily available and useful parameter for optimizing $J$ in our system, which is described in more detail in Section S1, Supporting Information. Identifying a stable TMP window is crucial for prolonged effectiveness of CF-MF because a reduction in TMP corresponds to declining flux. We performed process optimization by varying the feed concentration and feed flow rate as independent variables (Table S2, Supporting Information), with graphene concentration in the permeate stream and pressure sensor readings serving as dependent variables used to calculate TMP.

This optimization identified an ideal combination of high channel flow rate, low permeate flow rate, and low feed concentrations (**Figure 2**). Under these conditions, the channel flow provides a sweeping effect that dislodges poorly exfoliated graphitic particles and minimizes the formation of a dense polarization layer at the membrane surface (Figure 2a). In this stable operating regime, the polarization layer remains sufficiently porous to allow cross-flow of graphene nanosheets into the permeate stream (Figure 2b). On the other hand, once a dense polarization layer accumulates, only solvent molecules can penetrate the membrane surface (Figure 2c). To visualize the polarization layer, a representative CF-MF lumen was imaged with scanning electron microscopy (SEM) following prolonged graphene separation (Figure 2d). SEM reveals a highly open microstructure at the exterior surface of the lumen (Figure 2e), whereas the interior lumen surface is coated with a dense polarization layer of graphitic particles (Figure 2f).

In addition to determining flow rate conditions that lead to a high and stable TMP, the feed concentration ($C_{Feed}$) has to be optimized for efficient and prolonged CF-MF of graphene. Successful separation was initially possible without dilution, but rapid fouling soon occurred along with a decline in TMP (Figure S2a,b, Supporting Information). This decline can be attributed to the formation of the dense polarization layer (Figure S3, Supporting Information). After diluting $C_{Feed}$ to 0.30 mg $mL^{-1}$ with pure ethanol, minimal fouling was observed, and the TMP remained stable at ≈1 PSI for hours (Figure S2c,d, Supporting Information). In summary, we found TMP = (0.17–0.30) $P_f$ to be the ideal pressure window for CF-MF, where $P_f$ is the feed pressure (Figure S2e, Supporting Information).

### 2.3. Characterization of Graphene Nanosheets Separated by Cross-Flow Microfiltration

The size of the graphene nanosheets separated by CF-MF was characterized with a combination of microscopy and light scattering techniques (**Figure 3**). First, atomic force microscopy (AFM, Figure 3a) was used to obtain distributions of nanosheet length values (Figure 3b)—defined here as the square root of the flake area ($\sqrt{A_{flake}}$)—along with flake thickness ($t_{flake}$, Figure 3c). From AFM of the CBS control sample, we found that $<\sqrt{A_{flake}}>$ = 104.2 nm and $<t_{flake}>$ = 3.4 nm. Meanwhile, from the CF-MF permeate, CFF graphene nanoflakes exhibited comparable sizes of $<\sqrt{A_{flake}}>$ = 107.3 nm and $<t_{flake}>$ = 2.3 nm ($n$ = 50–100).

Dynamic light scattering (DLS) was also employed for rapid screening of CF-MF process streams (Figure 3d). Although the nominal sizes obtained via DLS are quantitatively unreliable for anisotropic nanoparticles,[44] DLS still provides a relative comparison of the size scale of CF-MF process streams. Successive measurements of the particle size distributions indicated a shift toward smaller particle sizes after CF-MF. Meanwhile, the autocorrelation functions of the coarse feed and retentate dispersions showed evidence of aggregates, with evident variability between repeated measurements that is consistent with high polydispersity.

Here, we quantify monodispersity using two metrics from DLS analysis: the cumulant particle size (Z-Average) and polydispersity index (PDI), both of which are derived for colloidal materials by Ragheb et al. (see also Section S3.4, Supporting Information).[45] The CBS control sample processed at ≈10500 rcf exhibited Z-Average = 273 nm and PDI = 0.179. Based on this result and the findings of Ragheb et al., we set Z-Average

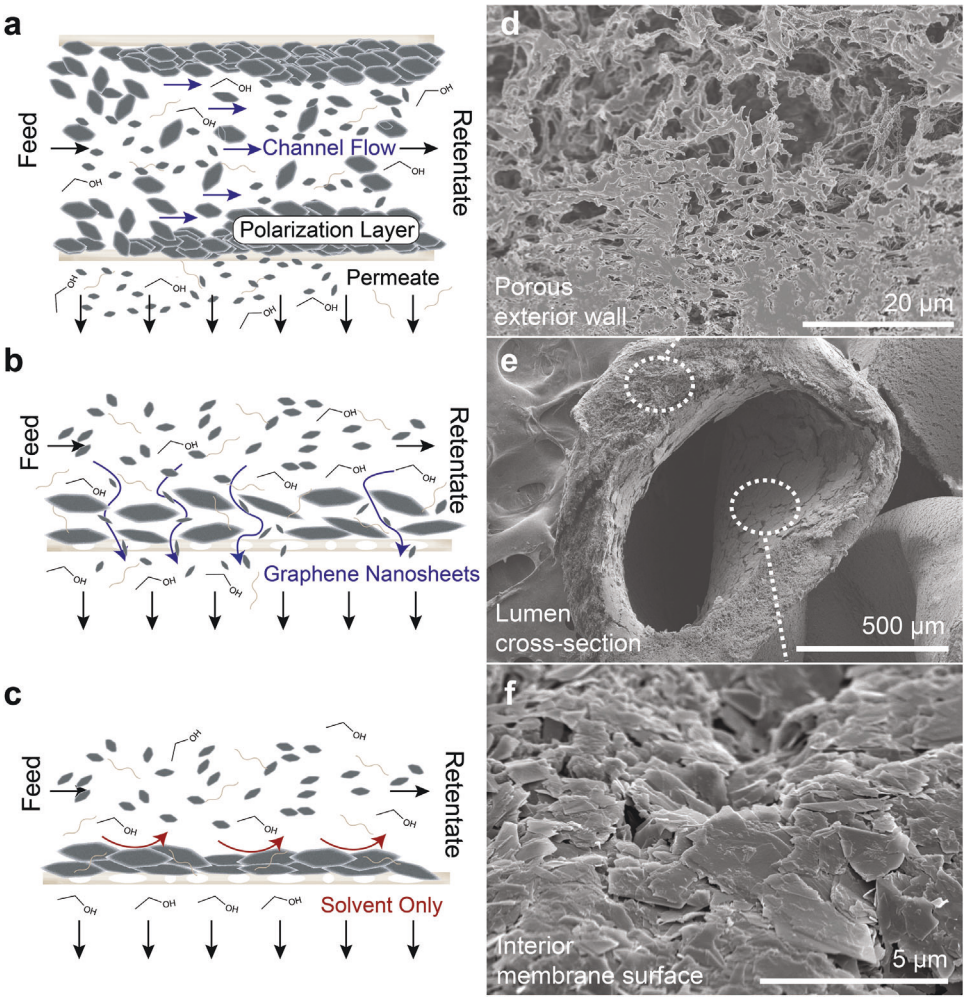


**Figure 2.** Polarization layer formation during cross-flow filtration of graphene. a) During CFF, shear-mixed dispersions flow turbulently through the hollow fiber membrane in a blunted parabolic profile. b) At high channel flow rates and low feed stream concentrations, the polarization layer remains sufficiently porous to enable continuous collection of graphene nanosheets through the permeate. c) At low channel flow rates and/or high feed stream concentrations, a compact polarization layer forms that leads to membrane fouling. Post-mortem scanning electron microscopy shows: d) Highly porous microstructure of the unobstructed polysulfone membrane, e) zoomed-out view of the fouled lumen cross-section, and f) the graphite polarization layer that forms on the lumen interior surface after extended operation.

= 400 nm and PDI = 0.300 as the criteria for monodispersity. Notably, the DLS analysis values are highest for the retentate, showing an enrichment in poorly exfoliated graphite (Figure 3d-iii.) In contrast, the CF-MF permeate dispersion of graphene nanosheets shows the lowest Z-Average = 342 nm and PDI = 0.261, meeting the monodispersity criteria.

To further illustrate that our DLS analysis threshold is a predictor of downstream material performance, we spin-coated and compared the conductivity of graphene films from the retentate and feed streams of CF-MF. The retentate sample, which had PDI > 0.300 and Z-Average > 400 nm, also exhibits an inferior film conductivity of $c = 3.34 \times 10^3$ S m$^{-1}$ compared to the CF-MF permeate samples ($c = 2.03 \times 10^4$ S m$^{-1}$). Finally, Raman spectroscopy of the constituent films (Figure S4, Supporting Information) shows the evolution of a shoulder on the 2D peak in the retentate-derived film that is characteristic of microcrystalline graphite versus the narrow, symmetric 2D band in the permeate-derived film.[46]

To demonstrate scalability, the CF-MF process was then translated to the pilot scale with an apparatus built in-house that increased the membrane area tenfold and the processing volume 20-fold, all while keeping the filter material, pore size, and $C_{\text{Feed}}$ constant (Tables S1 and S2, Supporting Information). The pilot-scale apparatus also utilized high-flow peristaltic pumps that enabled $\gamma_w$ to be increased to 16 000 s$^{-1}$ (Equation (S1), Supporting Information) and the volumetric throughput ($T_{\text{volumetric}}$) to 15 L h$^{-1}$ (Figure S5, Supporting Information). This throughput represents a ≈2 orders of magnitude advantage compared to conventional centrifugation. At the pilot scale, we also observed higher TMP stability, particularly that ≈1 gallon of graphene dispersion could be processed in 15 min with minimal fluctuation in TMP (Figure S2f, Supporting Information).

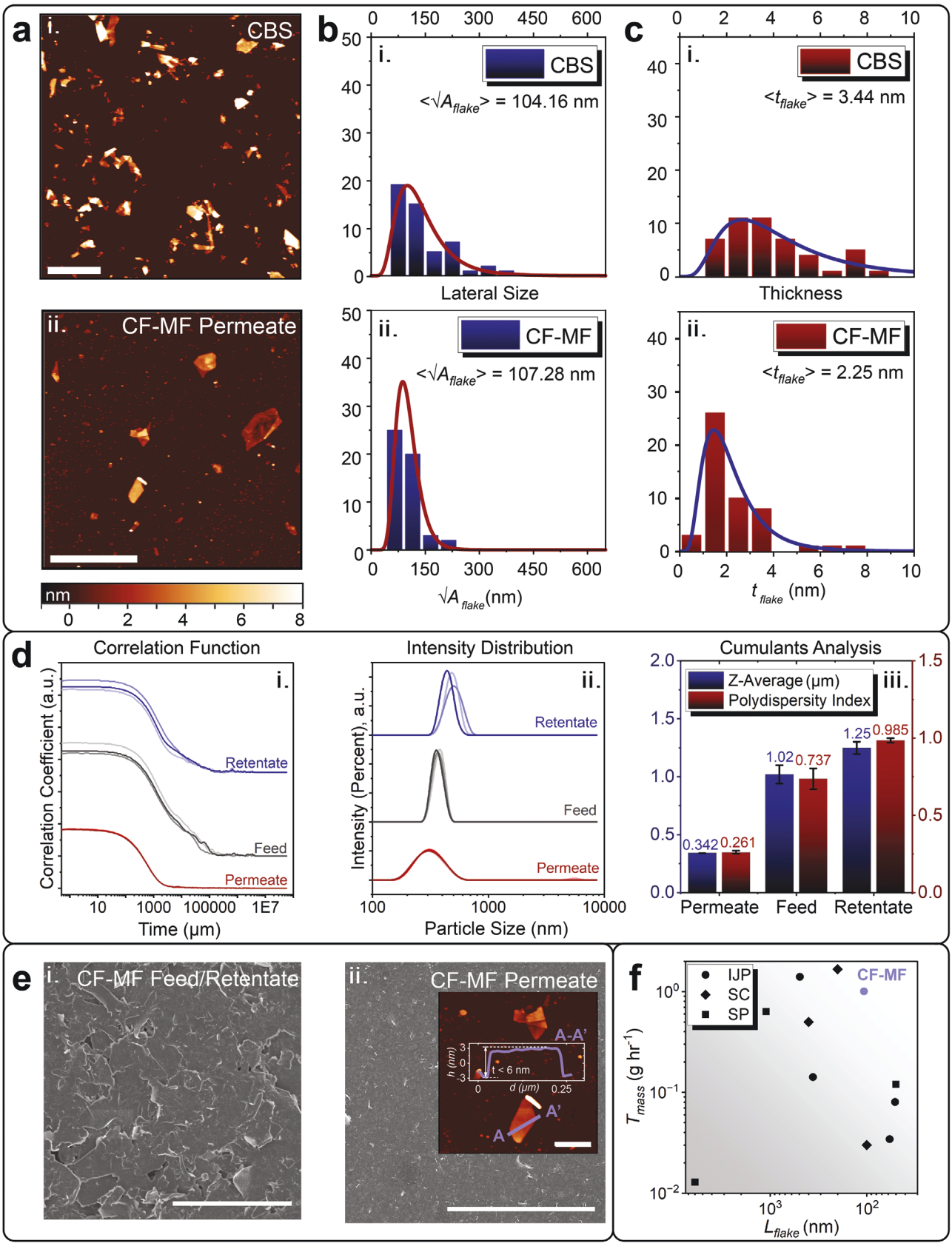

Since ultimately the output graphene mass per unit time is the most important scalability metric for graphene manufacturing, the mass throughput ($T_{mass}$) versus the lateral size of separated graphene flakes ($L_{flake}$) is compared between this work and previously reported separation approaches in Figure 3f. Here, "SC" = spin-coating, "SP" = screen printing, and "IJP" = inkjet printing; these material printing techniques will be revisited in Section 2.5. For this comparison, $L_{flake}$ is based on the graphene flake length determined by microscopy using the optimal centrifugation conditions specified by the authors (i.e., the reported best result for the target application). Each of these prior works had also successfully printed graphene into thin films with electrical conductivities $\geq 10^3$ S m$^{-1}$ as summarized in Table S3, Supporting Information. Overall, this comparison shows that CF-MF is state-of-the-art in terms of $T_{mass}$ with additional advantages that will be discussed below.

### 2.4. Cross-Flow Ultrafiltration for Material Recycling

Following separation of graphene, additional processing steps are still required to isolate graphene nanosheets including centrifuge-based flocculation, rinsing, and solvent removal. Upon implementation of pilot-scale CF-MF, these post-separation processing steps become the bottleneck in the production of graphene nanosheets. Therefore, we explored the use of hollow fiber membranes with nanoscale pore sizes rated for CF-UF to selectively remove ethanol and EC from the CF-MF permeate. This approach not only facilitates efficient removal and recycling of ethanol and EC but also simplifies post-separation processing. Since the molecular weight of 4 cP EC is ≈20 kDa,[47] CF-UF filter modules were tested with a nominal molecular weight cutoff of 500–750 kDa (≈10.9–12.5 nm).[48] Full parameters for the CF-UF studies are outlined in Tables S1 and S2, Supporting Information. The CF-MF permeate became the feed dispersion for CF-UF, with ethanol and EC traversing the nanoporous membrane into the CF-UF permeate. Subsequently, rotary evaporation allowed for separation and recovery of ethanol and EC, with the recycled EC showing viscosity comparable to the EC raw material (Figure S6, Supporting Information). This result suggests that minimal EC polymer scission occurred during shear-mixing and subsequent CF-MF processing, allowing EC to be reused for further graphene exfoliation.

The retentate from the CF-UF process is a concentrated dispersion of graphene nanosheets. The volumetric concentration factor ($C_v$) of the process depends on the volume of feed dispersion ($V_{feed,\ initial}$) and the volume of permeate dispersion ($V_{permeate}$) collected from the CF-UF permeate, as shown in Equation (2):[49]

$$C_v = \frac{V_{feed,\ initial}}{\left(V_{feed,\ initial} - V_{permeate}\right)} \quad (2)$$

The CF-UF experiments targeted $C_v = 10$. Afterward, the concentrated CF-UF retentate was flocculated into a solid graphene nanocomposite powder for comparison with a control sample of the CF-MF permeate that did not undergo CF-UF. Thermogravimetric analysis of the flocculated graphene/EC powders showed that after CF-UF, the mass ratio of graphene to EC increased from 40 to 60 wt% (Figure S7, Supporting Information), thus confirming that excess EC was removed from the dispersion during CF-UF. Overall, the sequential application of CF-MF and CF-UF offers a dual-function, continuous-flow processing scheme for 1) isolating monodisperse graphene nanosheets and 2) recovering ethanol and EC for reuse. In previous demonstrations of CFF, at least one of the process streams is discarded as waste. In contrast, we have utilized all three CFF process streams to not only isolate graphene nanosheets but also to recycle poorly-exfoliated graphite, EC, and ethanol.

### 2.5. Electronic Performance of Graphene Nanosheets Following Cross-Flow Microfiltration

For this work, we are defining graphene quality by its downstream performance in electronic-grade films, which have a reliable figure of merit (i.e., film conductivity) that is easily compared across applications. It should be noted that multi-layer graphene nanoflakes with sizes comparable to our CFF-derived graphene comprise the highest market fraction for graphene and its derivatives (i.e., 52% of the global graphene market, projected at $180 million as of 2022).[50]

The CFF-derived graphene/EC powder shown in Figure S8a, Supporting Information, was formulated into printable conductive inks to assess the electronic performance of the graphene nanosheets (**Figure 4**). Conductive graphene inks were prepared and tested for AJP (Figure 4a) and IJP (Figure 4b) using formulations adapted from previous reports.[51,52] Specifically, the AJP and IJP inks employed a 90:10 ratio of ethanol:terpineol and an 80:15:5 ratio of cyclohexanone:terpineol:diethylene glycol monomethyl ether, respectively. Rheological measurements indicate that the IJP ink is more viscous than the AJP ink, as expected (Figure 4c).

After printing, the substrates were thermally cured in ambient conditions at 350 °C for 30 min to decompose the EC polymer. Following curing, the film conductivity was measured to be $> 10^4$ S m$^{-1}$ for both inks (Figure 4d), which is consistent with previous results.[51,52] Optical microscopy confirmed well-defined

**Figure 3.** Characterization of graphene after cross-flow microfiltration (CF-MF). a) Atomic force microscopy (AFM) of a control sample obtained by i) centrifuge-based sedimentation (CBS) and ii) a CF-MF permeate sample. Scale bars are 1 µm. b) AFM lateral size and c) thickness histograms for graphene nanoflakes from i) CBS and ii) CF-MF ($n$ = 50–100). d) Dynamic light scattering offers a rapid-screening tool for relative comparison of CFF process streams. i) Autocorrelation functions and ii) intensity-weighted particle size distributions indicate less variation in successive measurements of the CFF permeate, while iii) cumulants analysis indicates a lower polydispersity index and particle size (Z-Average) for the permeate samples. e) Scanning electron microscopy (SEM) of films prepared from i) indistinguishable CF-MF feed and retentate dispersions and ii) CF-MF permeate dispersions, with inset AFM nanoflake detail. Scale bars are 10 µm for SEM and 0.25 µm for inset AFM. f) Comparison of mass throughput ($T_{mass}$) of CF-MF as a separation technique compared to reports of printed LPE graphene films with conductivities $>10^3$ S m$^{-1}$, using reported lateral nanoflake sizes ($L_{flake}$) obtained via microscopy. For our work (CF-MF), $L_{flake} = <\sqrt{A_{flake}}> \cong 107$ nm from AFM. "SC," "SP," and "IJP" stand for spin-coating, screen printing, and inkjet printing, respectively.

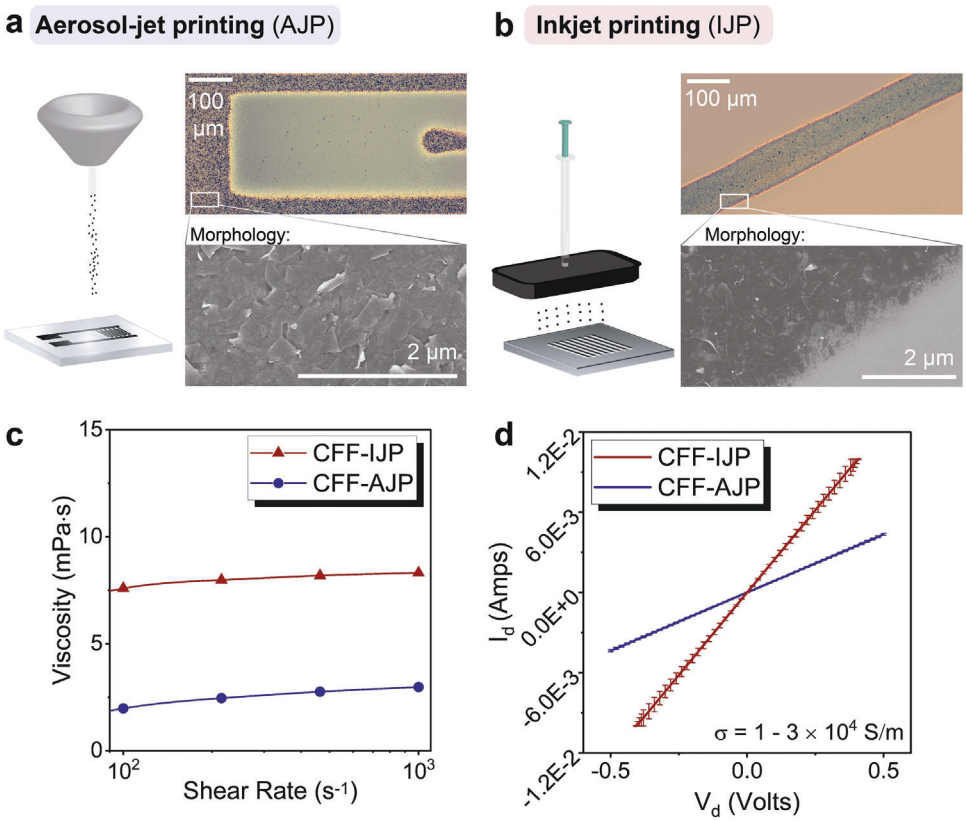


**Figure 4.** Graphene processed by CF-MF yields printable inks with high electrical conductivity. CF-MF graphene/EC was formulated into inks that are compatible with a) aerosol-jet printing (CFF-AJP) and b) inkjet printing (CFF-IJP). c) Viscosity as a function of shear rate for the two printable graphene inks. The viscosity can be further tuned by adjusting the solids loading in the ink formulation. d) After printing and removing EC via thermal decomposition, the graphene films show an ohmic response with electrical conductivities exceeding $10^4$ S $m^{-1}$.

printed features, and SEM showed the formation of dense, percolating films for both IJP and AJP. While the graphene/EC powders used to formulate each ink were compositionally identical (Figure S8b, Supporting Information), the AJP printed features showed marginally lower conductivity due to the formation of rougher graphene films by aerosolization.

Spectroscopic characterization of CFF-derived films further confirmed the physicochemical characteristics of high-quality graphene. For example, Raman spectroscopy performed after thermal decomposition of EC (Figure S8c, Supporting Information) indicates the characteristic D (1348 $cm^{-1}$), G (1580 $cm^{-1}$), and 2D (2699 $cm^{-1}$) bands of graphene.[53] A Gaussian fit of the Raman spectrum reveals full-width at half-maximum (FWHM) values of 42.8, 25.3, and 80.4 $cm^{-1}$ for the D, G, and 2D peaks, respectively, and an $I_D/I_G$ ratio of 0.354. These values are consistent with prior reports of graphene nanosheets exfoliated in ethanol with EC.[51,52] To further justify the quality of the printed material, we note that graphene nanoflake films with similar metrics have performed well in printed electronic applications including an aerosol-jet-printed COVID-19 immunosensor ($I_D/I_G \approx 0.33$ and FWHM(2D) ≈80 $cm^{-1}$).[40] X-ray photoelectron spectroscopy (Figure S8d, Supporting Information) characterization further confirms physicochemical characteristics of graphene that are consistent with prior reports.[51,52] Since these metrics remained constant following repeated filtration cycles, we conclude that the graphene quality remains invariant for the duration of the CFF module operating lifetime. Overall, these results confirm that CFF-derived graphene nanosheets are physically, chemically, and electronically equivalent to traditional centrifuge-based processing, which implies that they can be directly employed in high-performance graphene applications.

### 2.6. Life Cycle Assessment and Techno-Economic Analysis

Significant drawbacks of the incumbent CBS approach for 2D nanosheet separation include its significant capital equipment costs, labor requirements, and energy consumption. Using a functional unit of 1 g of graphene, we performed a holistic comparison of the CFF/CBS separation processes using LCA to evaluate CFF sustainability gains for scale-up (**Figure 5**). This analysis was based on the integration of CF-MF and CF-UF depicted in Figure 5a ("CFF") and conventional CBS paired with CF-UF for ethanol/EC recycling (Figure S9, Supporting Information).

Regarding key assumptions, we note that to ensure the most objective comparison possible, we only considered instrument runtime (i.e., not cleaning time) in the calculations for yield and throughput. Based on our experimentation, the CFF module lifetime is ≈6 weeks. Thus, we have overestimated an annual inventory of 10 CFF modules weighing ≈270 g each. Detailed informa-

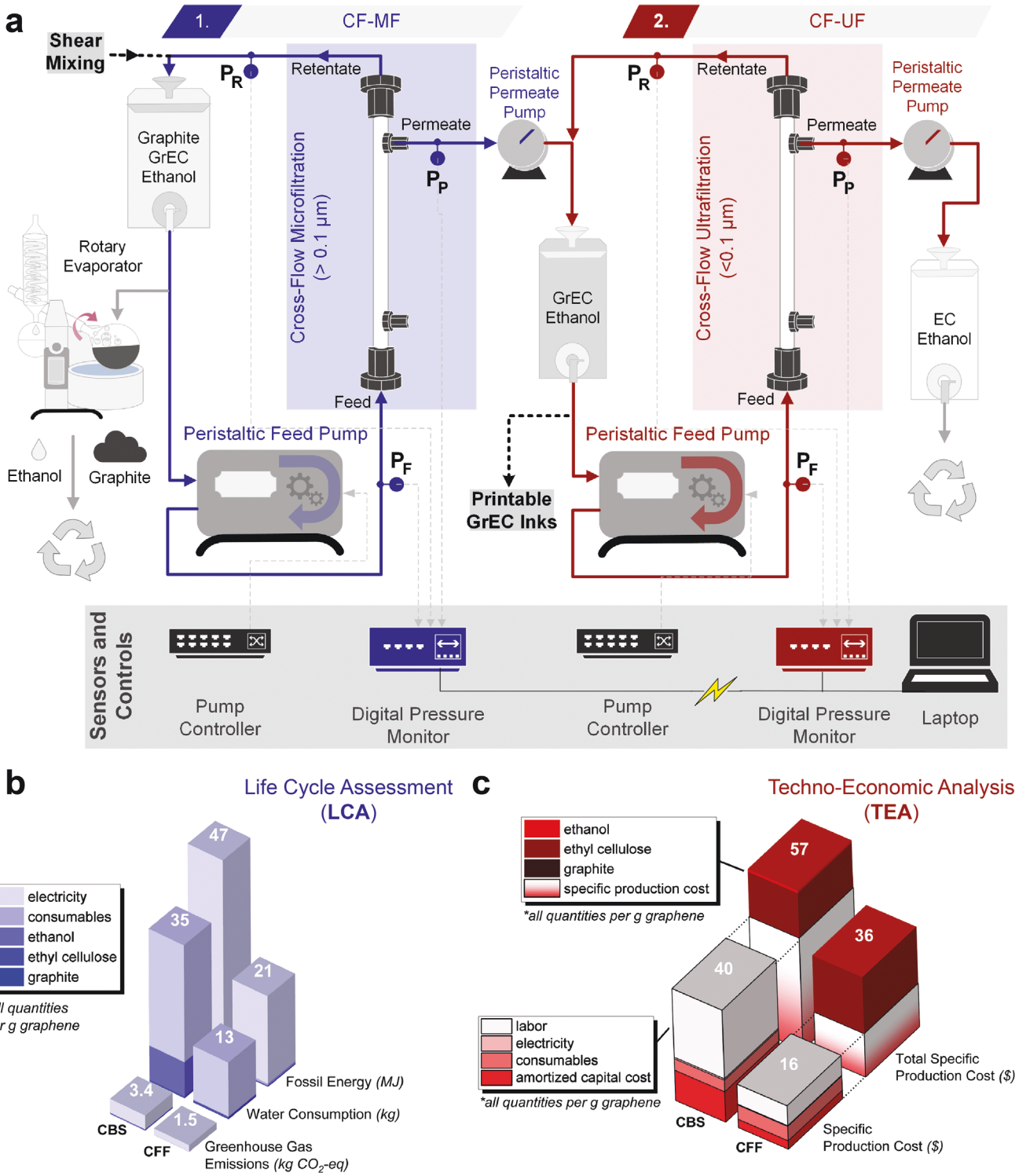


**Figure 5.** Integrated cross-flow filtration (CFF). a) Schematic overview of an idealized pilot-scale CFF apparatus. CF-MF and CF-UF operate simultaneously to separate graphene and recover raw materials, respectively. b) Life cycle assessment (LCA) and c) techno-economic analysis (TEA) results for CFF in comparison to centrifuge-based sedimentation (CBS). The dashed lines in (c) indicate a breakdown of the specific production cost without including the cost of raw materials. At the 1 L scale, cross-flow filtration improves environmental impacts of graphene manufacturing by 57–63%, primarily due to reduced electricity consumption. Specific production cost of graphene is improved by 72% (37% with materials) due to decreased labor and capital cost.

tion regarding all relevant values and assumptions used in LCA is included in Section S15, Supporting Information, including environmental and techno-economic parameters from the literature (Table S4, Supporting Information) and inventory of materials (Table S5, Supporting Information). Tabulated results of environmental impacts per 1 g of graphene are provided in Table S6, Supporting Information.

Overall, LCA calculations for greenhouse gas emissions, fossil energy usage, and water consumption reveal reductions of 57%, 56%, and 63%, respectively, for CFF compared to conventional CBS processing (Figure 5b). Lower electricity consumption with CFF is an important driver behind its lower greenhouse gas emissions and fossil energy usage. In addition, the ability of CFF to recycle ethanol and EC reduces water consumption due to the wet milling that is used in modern ethanol production. Although centrifugation offers higher material conversion efficiency due to the additional dilution of the feed stream prior in CF-MF, the environmental impacts of consumables for both processes account for less than 5% of the total environmental effects of graphene manufacturing.

TEA further illustrates the economic benefits of CFF compared to CBS, with specific production costs being reduced by 72% before material costs are included and still being reduced by 37% including materials (Figure 5c). The primary drivers for the economic advantage of CFF are reduced labor costs and amortized capital equipment costs (Table S7, Supporting Information). Although the materials costs are currently higher for CFF, further optimization of the recycling step is likely to address this issue, resulting in additional improvements in the total specific production cost of graphene via CFF. Finally, we explore the effect of variable scenarios (e.g., increased fouling leading to higher CFF module turnover, increased run time, and including washing/regeneration process) on the LCA/TEA results in Section S20, Supporting Information.

## 3. Conclusion

In this work, we have demonstrated a continuous-flow, high-throughput, and energy-efficient post-exfoliation graphene separation process based on CFF. Specifically, we have inverted the traditional CFF paradigm by isolating the permeate containing size-refined 2D materials, whereas previous reports collected the retentate and discarded the permeate. Furthermore, by changing the membrane pore size from the microfiltration to the ultrafiltration regime, our CFF process not only addresses the centrifugal separation bottleneck for solution-exfoliated graphene but also facilitates recovery and recycling of excess solvents and stabilizing polymers. This CFF process features a polydisperse, shear-mixed mixture flowing tangentially to the surface of a porous membrane, minimizing material buildup on the membrane surface and avoiding entrapment of larger particles in the membrane interior. In CF-MF, graphene nanosheets traverse the membrane pores via cross-flow for collection in a monodisperse, nanoscale permeate dispersion. These permeate graphene nanosheets show comparable size characteristics and electrical conductivity to centrifuged samples, but with orders of magnitude improvement in manufacturing throughput. Our sequential use of CF-MF and CF-UF allows us to not only isolate 2D materials, but also to harvest other raw materials for reuse (e.g., poorly exfoliated bulk material, solvent, and stabilizer molecules), which are typically discarded. This combined approach further differentiates our work from prior reports and offers major sustainability advantages. In particular, integrated CF-MF and CF-UF results in reduction of greenhouse gas emissions, fossil energy usage, water consumption, and specific production costs by 57%, 56%, 63%, and 72%, respectively. Since this methodology is based purely on separation by size (as opposed to chemical composition or other materials properties), it should be generalizable to other 2D materials, thus enabling sustainable manufacturing for the broad class of van der Waals layered solids.

## 4. Experimental Section

*Materials*: Graphite flakes (+100 mesh, Catalog No. 332 461), ethyl cellulose (EC, 4 cP, 5% in 80:20 toluene:ethanol, Catalog No. 200 646), cyclohexanone (Catalog No. 398 241), and terpineol (Catalog No. 86 480) were all purchased from MilliporeSigma (St. Louis, MO). 200-proof ethanol for all experiments was manufactured by Decon Laboratories (King of Prussia, PA) and purchased from Fisher Scientific (Waltham, MA, Catalog No. 04-355-223). Diethylene glycol monomethyl ether was manufactured by TCI Chemicals (Tokyo, JPN) and purchased from Fisher Scientific (Catalog No. M053725ML). For CFF, polysulfone hollow fiber filtration modules from Cytiva (Marlborough, MA) with pore size cutoffs ranging from 500 000 Da (Catalog No. UFP-500-DMA) to 0.65 µm (Catalog No. CFP-6-D-3MA and Catalog No. CFP-6-D-5A) were used.

*Liquid-Phase Exfoliation*: Graphite was shear mixed at high speeds using an LM5-A Lab Mixer (Silverson Machines, East Longmeadow, MA). EC was pre-dissolved into ethanol (1% w/v) for each batch using a stir bar at room temperature. The polymer/solvent solution was then combined with the bulk graphite powder (10% w/v graphite) in a 2 L jacketed beaker (Fisher Scientific Catalog No. CG110306). The vessel was cooled with a recirculating chiller (Thermo Fisher, Waltham, MA) to 5 °C, and the mixture of graphite powder and EC/ethanol was shear mixed at 10230 rpm for 2 h. The dispersions were allowed to settle overnight before filtration experiments were performed. For centrifuge control samples, the resulting dispersion was centrifuged at ≈10 500 rcf for 30 min using an Avanti-J26 XPI centrifuge equipped with a JLA-8.100 rotor and 1 L polypropylene bottles (Beckman Coulter, Brea, CA), and the supernatant containing graphene nanosheets was extracted for processing and analysis.

*General Cross-Flow Filtration Procedure*: At the laboratory scale, filtration experiments were carried out using an ÄKTA Flux s semi-automated tangential flow filtration/CFF system (Cytiva, Product No. 29 038 437) equipped with two peristaltic pumps—one for the feed dispersion and one for the permeate dispersion. Brand-new hollow fiber modules were mounted, plumbed, and washed with deionized water for 5–120 min prior to use following manufacturer instructions with an ÄKTA Flux s tubing kit (Cytiva, Product No. 29 060 952). The hollow fiber filters were subsequently only washed with ethanol for 5 min with a feed pump flow rate of 0.200 L $min^{-1}$ and a permeate dispersion flow rate of 0.005 L $min^{-1}$ between runs. After draining, shear-mixed graphene dispersions were poured into the reservoir and stirred. During lab-scale trials, an optional transfer pump was used in diafiltration mode to replenish lost ethanol volume. The pressure and graphene concentration data were consistent across a minimum of $n = 3$ separate experiments, with or without separate CFF modules.

*Cross-Flow Microfiltration*: For CF-MF, the feed flow rate was first slowly increased to 70–100% of the maximum afforded by the pump (0.240–0.343 L $min^{-1}$). Next, the permeate flow rate was gradually increased toward a predetermined target parameter based on the membrane surface area (Tables S1 and S2, Supporting Information) until the TMP was maximized and stable. Across all CF-MF experiments, permeate flow rates were modulated over the range of 0.002–006 L $min^{-1}$. No retentate flow control was used during the process. The CF-MF filter modules were flooded and stored in an 80:20 mixture of deionized water and ethanol when not in use.

*Cross-Flow Ultrafiltration*: For CF-UF, the same procedure as CF-MF was applied with the following differences: 1) experiments were conducted in concentration mode to facilitate ethanol recovery; 2) higher permeate flow rates (e.g., 0.010 L $min^{-1}$) were attained while keeping the TMP in an acceptable range (i.e., <10 PSI for CF-UF membranes). After each permeate sample was collected, the filters were thoroughly rinsed with ethanol (feed flow rate = 0.200 L $min^{-1}$, permeate flow rate = 0.005 L $min^{-1}$) to remove excess material and solvent. Filter modules were rated with 500–750 kDa pore size, and CF-MF permeate was used as the feed dispersion for CF-UF experiments. In a standard experiment, 1 L of CF-MF permeate dispersion was reduced to 0.100 L by extracting 0.900 L of ethanol/EC solution as the CF-UF permeate. During filtration, a 0.250 L $min^{-1}$ feed flow rate and a 0.010 L $min^{-1}$ permeate flow rate were used. Afterward, the concentrated CF-UF retentate was decanted for further study.

*Rotary Evaporation*: Solids were recovered from CF-MF and CF-UF samples after loading the retentate or permeate dispersions into a R300 rotary evaporator (BUCHI Corporation, New Castle, DE) with a 50 °C heating bath, 10 °C condenser temperature, 250 rotations per minute, and 70–97 mbar applied to the column. Once dried, the solids were recovered by scraping the inside of the powder drying flask with a spatula and weighed. Thermogravimetric analysis was then used to determine the relative composition of the graphene/EC and EC solids.

*Ink Formulation*: When preparing printable conductive inks, CFF permeate dispersions containing graphene/EC were flocculated into solid powders using 4% w/v NaCl:$H_2O$, collected, washed with deionized water, and dried as previously reported.[51] The powders were then redispersed via bath sonication in an 80:15:5 v/v mixture of cyclohexanone, terpineol, and diethylene glycol monomethyl ether with 2% w/v graphene/EC solids. Immediately prior to printing, the inks were fed through a glass microfiber syringe filter (pore size = 0.70 µm). Meanwhile, for AJP experiments, the same CFF graphene/EC powders were redispersed in ethanol at a solid loading of 1% w/v via horn sonication using a ¼" tip at 40% amplitude for 10 min. Prior to printing, the dispersion was filtered through a glass microfiber syringe filter (pore size = 3.1 µm). 10% v/v terpineol was added to the ink vial, and the mixture was bath sonicated for 10 min.

*Film Deposition*: IJP experiments were carried out using a DMP-2850 material printer (FUJIFILM Dimatix Inc., Santa Clara, CA) equipped with 10 pL cartridges (Product No. DMC-11610, 20.4 µm nozzle). Detailed printing protocols, including the waveform and cartridge setting files, are available on the product page for MilliporeSigma Catalog No. #793 663. AJP experiments were carried out using an AJ200 material printer (Optomec, Albuquerque, NM, USA) using the following parameters: platen temperature was set to 60 °C, bath temperature was set to 30 °C, print speed was set to 5 mm $s^{-1}$, nitrogen sheath flow was set to 60 sccm, and nitrogen carrier gas flow rate was set to 15–22 sccm with an atomization current of 0.354 mA. After printing, the specimens were heated at 350 °C for 30 min using a box furnace to decompose the EC binder and increase film conductivity, as previously reported.[52]

*Life Cycle Assessment and Techno-Economic Analysis*: LCA is based on ISO 14 040/44 standards.[54,55] Meanwhile, TEA examines the energy, material, and water consumption in addition to the cost performance of each graphene production process based on a material and energy flow analysis and an annualized cost approach.[56,57] The functional unit used for comparison purposes was 1 g of graphene, and all costs were defined by the US dollar ($) in 2021. The specific production cost ($C_p$, $\$\ g^{-1}$) of graphene was calculated through an annualized cost approach, as shown in Equation (3):

$$C_p = \frac{C_{ac} + C_{O\&M}}{Y} + C_m \quad (3)$$

The annualized capital costs ($C_{ac}$) were calculated based on process lifetime ($n$, years) and discount rate ($r$) shown in Equation (4):

$$C_{ac} = C_c \times \left( \frac{r \times (1+r)^n}{(1+r)^n - 1} \right) \quad (4)$$

Raw material costs ($C_m$) for graphite, EC, and ethanol were determined based on a functional unit of 1 g graphene, whereas $Y$ is the annual graphene yield. The capital costs ($C_c$) of the two processes were assumed to be only the equipment purchase costs in this calculation. Meanwhile, the operating and maintenance expenses ($C_{O\&M}$) include the annual cost of consumables, electricity, and labor. All LCA and TEA parameters with full data and assumptions for graphene production are detailed in Tables S4–S7, Supporting Information.

## Supporting Information

Supporting Information is available from the Wiley Online Library or from the author.

## Acknowledgements

The National Science Foundation (NSF) supported this work through the Scalable Nanomanufacturing Program (NSF Award Number CMMI-1727846) and NSF MADE-PUBLIC Future Manufacturing Research Grant Program (NSF Award Number CMMI-2037026). J.R.D. also acknowledges the National Consortium for Graduate Degrees for Minorities in Engineering and Science (GEM) Fellowship co-administered by the 3M Company and Northwestern University. This work made use of the EPIC facility and Keck-II facilities of the Northwestern University NUANCE Center, which has received support from the Soft and Hybrid Nanotechnology Experimental (SHyNE) Resource (NSF ECCS-1542205), the MRSEC program (NSF DMR-1720139) at the Materials Research Center, the International Institute for Nanotechnology (IIN), the Keck Foundation, and the State of Illinois. This work also made use of the MatCI facility at Northwestern University, which was supported by the MRSEC program (NSF DMR-1720139). The authors also acknowledge Sonal Rangnekar for consultation on graphene ink development and Chen Ling for data analysis support.

## Conflict of Interest

The inkjet-printable graphene formulation is commercially available via a material transfer agreement between Northwestern University and MilliporeSigma.

## Author Contributions

J.R.D., J.-W.T.S., and M.C.H. conceived the idea. J.R.D, S.D.-A, L.E.C., J.-W.T.S., and M.C.H. designed the microfiltration experiments. J.R.D., L.E.C., and S.D.-A. prepared the graphene dispersions and performed the microfiltration experiments. J.R.D. and D.T. designed and performed the ultrafiltration experiments. D.R.C. and M.D. designed the lab-scale microfiltration setup, supported analysis of filtration data, and provided material resources. J.H.Q. performed filter de-fouling studies under guidance from J.R.D. J.R.D. and S.D.-A. developed and constructed the pilot-scale filtration setup, processed graphene inks, and performed physicochemical characterization with corresponding analysis. D.T. processed ultrafiltration samples via rotary evaporation for analysis and performed dynamic light scattering measurements. L.E.C. and N.X.W. performed aerosol-jet printing, and J.R.D. performed inkjet printing. J.H., L.E.C., and S.D.-A. performed profilometry, electrical characterization, and analysis of printed graphene films. S.D.-A. performed viscosity measurements and assisted with Raman analysis. J.-W.T.S. and D.T. performed scanning electron microscopy of microfiltration and ultrafiltration membranes. J.Z. conducted and analyzed the results of LCA and TEA under the guidance of J.B.D. J.R.D. and M.C.H. wrote the manuscript with input from all co-authors.

## Data Availability Statement

The data that support the findings of this study are available from the corresponding author upon reasonable request.

## Keywords

graphene, life cycle assessment, liquid-phase exfoliation, printed electronics, tangential flow filtration

Received: December 22, 2022
Revised: February 26, 2023
Published online: April 28, 2023

[1] A. K. Geim, K. S. Novoselov, *Nat. Mater.* **2007**, *6*, 183.
[2] A. Splendiani, L. Sun, Y. Zhang, T. Li, J. Kim, C. Y. Chim, G. Galli, F. Wang, *Nano Lett.* **2010**, *10*, 1271.
[3] I. Jo, M. T. Pettes, J. Kim, K. Watanabe, T. Taniguchi, Z. Yao, L. Shi, *Nano Lett.* **2013**, *13*, 550.
[4] J. N. Coleman, M. Lotya, A. O'Neill, S. D. Bergin, P. J. King, U. Khan, K. Young, A. Gaucher, S. De, R. J. Smith, I. V. Shvets, S. K. Arora, G. Stanton, H. Y. Kim, K. Lee, G. T. Kim, G. S. Duesberg, T. Hallam, J. J. Boland, J. J. Wang, J. F. Donegan, J. C. Grunlan, G. Moriarty, A. Shmeliov, R. J. Nicholls, J. M. Perkins, E. M. Grieveson, K. Theuwissen, D. W. McComb, P. D. Nellist, et al., *Science* **2011**, *331*, 568.
[5] K. R. Paton, E. Varrla, C. Backes, R. J. Smith, U. Khan, A. O'Neill, C. Boland, M. Lotya, O. M. Istrate, P. King, T. Higgins, S. Barwich, P. May, P. Puczkarski, I. Ahmed, M. Moebius, H. Pettersson, E. Long, J. Coelho, S. E. O'Brien, E. K. McGuire, B. M. Sanchez, G. S. Duesberg, N. McEvoy, T. J. Pennycook, C. Downing, A. Crossley, V. Nicolosi, J. N. Coleman, *Nat. Mater.* **2014**, *13*, 624.
[6] A. E. Del Rio Castillo, V. Pellegrini, A. Ansaldo, F. Ricciardella, H. Sun, L. Marasco, J. Buha, Z. Dang, L. Gagliani, E. Lago, N. Curreli, S. Gentiluomo, F. Palazon, M. Prato, R. Oropesa-Nuñez, P. S. Toth, E. Mantero, M. Crugliano, A. Gamucci, A. Tomadin, M. Polini, F. Bonaccorso, *Mater. Horiz.* **2018**, *5*, 890.
[7] W. Kong, H. Kum, S. H. Bae, J. Shim, H. Kim, L. Kong, Y. Meng, K. Wang, C. Kim, J. Kim, *Nat. Nanotechnol.* **2019**, *14*, 927.
[8] G. Hu, L. Yang, Z. Yang, Y. Wang, X. Jin, J. Dai, Q. Wu, S. Liu, X. Zhu, X. Wang, T. C. Wu, R. C. T. Howe, T. Albrow-Owen, L. W. T. Ng, Q. Yang, L. G. Occhipinti, R. I. Woodward, E. J. R. Kelleher, Z. Sun, X. Huang, M. Zhang, C. D. Bain, T. Hasan, *Sci. Adv.* **2020**, *6*, 5029.
[9] N. X. Williams, G. Bullard, N. Brooke, M. J. Therien, A. D. Franklin, *Nat. Electron.* **2021**, *4*, 261.
[10] G. Hu, J. Kang, L. W. T. Ng, X. Zhu, R. C. T. Howe, C. G. Jones, M. C. Hersam, T. Hasan, *Chem. Soc. Rev.* **2018**, *47*, 3265.
[11] A. G. Kelly, D. O'Suilleabhain, C. Gabbett, J. N. Coleman, *Nat. Rev. Mater.* **2022**, *7*, 217.
[12] C. Backes, T. M. Higgins, A. Kelly, C. Boland, A. Harvey, D. Hanlon, J. N. Coleman, *Chem. Mater.* **2017**, *29*, 243.
[13] J. Zhu, J. Kang, J. Kang, D. Jariwala, J. D. Wood, J. W. T. Seo, K. S. Chen, T. J. Marks, M. C. Hersam, *Nano Lett.* **2015**, *15*, 7029.
[14] C. Backes, B. M. Szydłowska, A. Harvey, S. Yuan, V. Vega-Mayoral, B. R. Davies, P.-L. Zhao, D. Hanlon, E. J. G. Santos, M. I. Katsnelson, W. J. Blau, C. Gadermaier, J. N. Coleman, *ACS Nano* **2016**, *10*, 1589.
[15] T. Carey, A. Alhourani, R. Y. Tian, S. Seyedin, A. Arbab, J. Maughan, L. Siller, D. Horvath, A. Kelly, H. Kaur, E. Caffrey, J. M. Kim, H. R. Hagland, J. N. Coleman, *npj 2D Mater. Appl.* **2022**, *6*, 3.
[16] P. G. Karagiannidis, S. A. Hodge, L. Lombardi, F. Tomarchio, N. Decorde, S. Milana, I. Goykhman, Y. Su, S. V. Mesite, D. N. Johnstone, R. K. Leary, P. A. Midgley, N. M. Pugno, F. Torrisi, A. C. Ferrari, *ACS Nano* **2017**, *11*, 2742.
[17] M. J. Large, S. P. Ogilvie, A. A. Graf, P. J. Lynch, M. A. O'Mara, T. Waters, I. Jurewicz, J. P. Salvage, A. B. Dalton, *Adv. Mater. Technol.* **2020**, *5*, 2000284.
[18] P. S. Fedotov, N. G. Vanifatova, V. M. Shkinev, B. Y. Spivakov, *Anal. Bioanal. Chem.* **2011**, *400*, 1787.
[19] L. Svarovsky, *Solid-Liquid Separation*, Butterworth-Heinemann, Oxford, England **2001**, p. 10.
[20] J. D. Robertson, L. Rizzello, M. Avila-Olias, J. Gaitzsch, C. Contini, M. S. Magoń, S. A. Renshaw, G. Battaglia, *Sci. Rep.* **2016**, *6*, 27494.
[21] S. K. R. Williams, J. R. Runyon, A. A. Ashames, *Anal. Chem.* **2010**, *83*, 634.
[22] H. Zhou, J. Tan, L. Yang, J. Wang, B. Ding, Y. Pan, X. Yu, M. Liu, C. Yang, L. Qiu, H. M. Cheng, B. Liu, *Sci. China Mater.* **2021**, *64*, 2739.
[23] G. D. Moeser, K. A. Roach, W. H. Green, T. A. Hatton, P. E. Laibinis, *AIChE J.* **2004**, *50*, 2835.
[24] J. Chen, Y. Li, L. Huang, N. Jia, C. Li, G. Shi, *Adv. Mater.* **2015**, *27*, 3654.
[25] A. Akthakul, A. I. Hochbaum, F. Stellacci, A. M. Mayes, *Adv. Mater.* **2005**, *17*, 532.
[26] J. F. Richardson, J. H. Harker, *Membrane Separation Processes*, Butterworth-Heinemann, Oxford, England **2002**, pp. 437–474.
[27] G. Belfort, R. H. Davis, A. L. Zydney, *J. Membr. Sci.* **1994**, *96*, 1.
[28] R. W. Field, D. Wu, J. A. Howell, B. B. Gupta, *J. Membr. Sci.* **1995**, *100*, 259.
[29] Y.-T. Lin, M. Sung, P. F. Sanders, A. Marinucci, C. P. Huang, *Sep. Purif. Technol.* **2007**, *58*, 138.
[30] K. C. Pradel, K. Sohn, J. Huang, *Angew. Chem., Int. Ed.* **2011**, *50*, 3412.
[31] S. Ohmori, T. Saito, B. Shukla, M. Yumura, S. Iijima, *ACS Nano* **2010**, *4*, 3606.
[32] S. G. Yim, Y. J. Kim, Y. E. Kang, B. K. Moon, E. S. Jung, S. Y. Yang, *Nanomaterials* **2018**, *8*, 959.
[33] F. J. Tölle, K. Gamp, R. Mülhaupt, *Carbon* **2014**, *75*, 432.
[34] C. Li, Y. Guo, L. Shen, C. Ji, N. Bao, *Chem. Eng. Sci.* **2019**, *200*, 127.
[35] A. T. Abdel-Motagaly, W. M. A. El Rouby, S. I. El-Dek, I. M. El-Sherbiny, A. A. Farghali, *Diamond Relat. Mater.* **2018**, *86*, 20.
[36] Y. T. Liang, M. C. Hersam, *J. Am. Chem. Soc.* **2010**, *132*, 17661.
[37] A. C. M. de Moraes, J. Obrzut, V. K. Sangwan, J. R. Downing, L. E. Chaney, D. K. Patel, R. E. Elmquist, M. C. Hersam, *J. Mater. Chem. C* **2020**, *8*, 15086.
[38] S. A. Farraj, E. Jabari, H. E. Naguib, T. Y. Chu, IEEE International Conference on Flexible and Printable Sensors and Systems (FLEPS), **2021**, https://doi.org/10.1109/FLEPS51544.2021.9469752.
[39] L. Kuo, V. K. Sangwan, S. V. Rangnekar, T.-C. Chu, D. Lam, Z. Zhu, L. J. Richter, R. Li, B. M. Szydłowska, J. R. Downing, B. J. Luijten, L. J. Lauhon, M. C. Hersam, *Adv. Mater.* **2022**, *34*, 2203772.
[40] C. C. Pola, S. V. Rangnekar, R. Sheets, B. M. Szydłowska, J. R. Downing, K. W. Parate, S. G. Wallace, D. Tsai, M. C. Hersam, C. Gomes, *2D Mater.* **2022**, *9*, 035016.
[41] R. R. Tafoya, M. A. Gallegos, J. R. Downing, L. Gamba, B. Kaehr, E. N. Coker, M. C. Hersam, E. B. Secor, *Microchim. Acta* **2022**, *189*, 123.
[42] R. R. Tafoya, A. W. Cook, B. Kaehr, J. R. Downing, M. C. Hersam, E. B. Secor, *Adv. Mater. Technol.* **2020**, *5*, 2000781.
[43] C. Backes, D. Campi, B. M. Szydłowska, K. Synnatschke, E. Ojala, F. Rashvand, A. Harvey, A. Griffin, Z. Sofer, N. Marzari, J. N. Coleman, D. D. O'Regan, *ACS Nano* **2019**, *13*, 7050.
[44] M. Lotya, A. Rakovich, J. F. Donegan, J. N. Coleman, *Nanotechnology* **2013**, *24*, 265703.
[45] R. Ragheb, U. Nobbmann, *Sci. Rep.* **2020**, *10*, 21768.
[46] C. Sole, N. E. Drewett, L. J. Hardwick, *Faraday Discuss.* **2014**, *172*, 223.
[47] H. Andersson, J. Hjärtstam, M. Stading, C. Von Corswant, A. Larsson, *Eur. J. Pharm. Sci.* **2013**, *48*, 240.
[48] L. Guo, P. H. Santschi, in *Environmental Colloids and Particles: Behaviour, Separation and Characterisation* (Eds.: K. J. Wilkinson, J. R. Lead), John Wiley & Sons, West Sussex, England **2007**, pp. 159–221.
[49] K. Scott, in *Handbook of Industrial Membranes – Absorption, Desorption and Extraction with Membranes*, Elsevier Advanced Technology, Oxford, UK **1998**, pp. 633–639.
[50] L. Lin, H. Peng, Z. Liu, *Nat. Mater.* **2019**, *18*, 520.

[51] E. B. Secor, P. L. Prabhumirashi, K. Puntambekar, M. L. Geier, M. C. Hersam, *J. Phys. Chem.* **2013**, *4*, 1347.
[52] K. Parate, C. C. Pola, S. V. Rangnekar, D. L. Mendivelso-Perez, E. A. Smith, M. C. Hersam, C. L. Gomes, J. C. Claussen, *2D Mater.* **2020**, *7*, 034002.
[53] J.-B. Wu, M.-L. Lin, X. Cong, H.-N. Liu, P.-H. Tan, *Chem. Soc. Rev.* **2018**, *47*, 1822.
[54] International Organization for Standardization, ISO 14040:2006 Environmental Management—Life Cycle Assessment—Principles and Framework, https://www.iso.org/standard/37456.html (accessed: December **2021**).
[55] International Organization for Standardization, ISO 14044:2006 Environmental Management—Life Cycle Assessment—Requirements and Guidelines, https://www.iso.org/standard/38498.html, (accessed: December **2021**).
[56] J. Zhang, H. Meerman, R. Benders, A. Faaij, *Energy* **2021**, *224*, 120049.
[57] T. Kuramochi, A. Ramírez, W. Turkenburg, A. Faaij, *Prog. Energy Combust. Sci.* **2012**, *38*, 87.